Corrosion Science 65 (2012) 214–222

Contents lists available at SciVerse ScienceDirect

Corrosion Science

journal homepage: www.elsevier.com/locate/corsci

Benzotriazole as a volatile corrosion inhibitor during the early stage of copper corrosion under adsorbed thin electrolyte layers

Zhenyu Chen *, Ling Huang, Guoan Zhang, Yubing Qiu, Xingpeng Guo

School of Chemistry and Chemical Engineering, Huazhong University of Science and Technology, Wuhan 430074, China

ARTICLE INFO

Article history:
Received 4 June 2012
Accepted 9 August 2012
Available online 17 August 2012

Keywords:
A. Copper
B. AFM
B. EIS
B. XPS
C. Neutral inhibition
C. Atmospheric corrosion

ABSTRACT

The inhibition effect of benzotriazole (BTAH) during the early stage of copper corrosion under adsorbed thin electrolyte layers (ATEL) was investigated. Electrochemical data show that BTAH suppressed the anodic corrosion reaction and inhibited copper corrosion under ATEL. The surface was examined by using a scanning electron microscopy, *in situ* atomic force microscopy, X-ray photoelectron spectroscopy, and attenuated total reflectance Fourier-transform infrared measurements. The inhibition of BTAH is attributed to its quick interaction with Cu(0) that formed a thin protective film in non-corroded areas and interaction with Cu(I) that formed a complex on Cu_2O substrate in defect sites.

1. Introduction

Copper is susceptible to atmospheric corrosion caused by O_2 and trace amounts of atmospheric pollutants such as Cl^- and CO_2. Atmospheric corrosion generally occurs under thin electrolyte layers (TEL) or adsorbed thin electrolyte layers (ATEL). The thickness of ATEL is usually less than 10 μm, when relative humidity (RH) is between 65% and 100% [1–3]. Several investigations on metal or alloy corrosion under TEL (thickness >10 μm) have been reported in the past decades [4–8]. However, experimental studies on metal or alloy corrosions under ATEL using conventional electrochemistry methods are very limited [1,9].

Several methods exist for preventing the atmospheric corrosion of copper. Among them, volatile corrosion inhibitor (VCI) is the most effective and affordable for industrial use. In recent years, VCI rapidly developed, and was extensively applied as an advanced corrosion-resistant material [10–13]. The main advantage of VCI compared with conventional corrosion control methods is its gas-phase transport that enables metallic surfaces to be reached. The VCI film is very thin and does not interfere with subsequent use or treatment of the protected surface [14]. The VCI film that adsorbs on the metal surface by means of physisorption or chemisorption may change the rate of electrochemical reactions such as the dissolution of metal and the reduction of oxygen [15]. However, no report has been made about the effect of corrosion inhibition of the inhibitor on metal under ATEL using conventional electrochemistry methods and *in situ* surface analysis techniques. Therefore, the study of inhibition effect on copper corrosion under ATEL is significant.

Benzotriazole (BTAH) and its derivatives are widely used to protect copper and its alloys from corrosion, which are, specifically, atmospheric copper corrosion protection and aqueous phase protection [16–24]. Although BTAH has been in use for a long time and numerous investigations have focused on the mechanism of BTAH interacting with copper in the aqueous phase, the mechanism of this compound as a copper inhibitor under ATEL is not completely clear, especially during the early stage.

Using electrochemical measurement, this paper studies the inhibition of copper corrosion by BTAH as VCI during the early stages of corrosion under ATEL. The adsorption of BTAH on the copper surface was measured by *in situ* atomic force microscopy (AFM) and by scanning electron microscopy (SEM). Interactions of BTAH with copper were examined by X-ray photoelectron spectroscopy (XPS) and by attenuated total reflectance Fourier-transform infrared (ATR-FTIR) measurements. The purpose of this study is to verify the film formation process and its inhibition mechanism under ATEL. To demonstrate the practical significance of the experiment, the addition of BTAH was carried out when copper was undergoing corrosion rather than before the film formation process.

2. Experimental

2.1. Materials and solutions

Commercially pure copper (99.99 wt.%, Aladdin Chemical Plant, China) was used in this study. The specimens (3.0 mm × 5.0 mm × 7.0 mm) were sealed using epoxy resin with 0.15 cm^2

* Corresponding author. Tel.: +86 27 87543432; fax: +86 27 87543632.
E-mail address: chenzhenyu@mail.hust.edu.cn (Z.Y. Chen).

0010-938X/$ - see front matter © 2012 Elsevier Ltd. All rights reserved.
http://dx.doi.org/10.1016/j.corsci.2012.08.019

exposed areas, and were employed in electrochemical tests as the working electrode (WE) and the counter electrode (CE). The specimens with 5 mm × 5 mm × 1 mm dimensions were used for AFM, XPS, ATR-FTIR, and SEM analysis. All test surfaces were ground with 1200 grit silicon carbide paper, and polished with 1.5 μm diamond pastes and 0.3 μm Al_2O_3 under N_2 protection. The surfaces were then ultrasonically washed with deionized water, degreased with ethanol, and dried with N_2. All solutions were prepared using analytical grade reagents and deionized water.

2.2. Design of the experimental set-up

For the experiment on the atmospheric corrosion of copper, the electrolyte was in the form of ATEL. ATEL is an extremely thin layer, thus resulting in considerable difficulty in electrochemical measurements [1]. To study the corrosion inhibition mechanism of BTAH for copper under ATEL by the electrochemical method, an experimental set-up was developed. Fig. 1 shows the schematic diagram of the set-up.

A three-electrode cell system was used for the electrochemical tests of copper in the absence and in the presence of BTAH in a closed container that contained aqueous glycerin solution. The method of obtaining 30–98% constant RH at 0–70 °C temperature in relatively small containers by means of aqueous glycerin solution is proven to be feasible [25]. Numerous pores were drilled on the baffle above the solution to maintain RH of the closed container. The three-electrode cell had two identical copper billets with the upper end surface size of 3 mm × 5 mm. The copper billets, which were used as WE and CE, were isolated with the epoxy resin, and their distances were 0.5 mm. Two copper wires were welded to the two electrodes to ensure electrical connection for the electrochemical measurements. A hole with a diameter of 2 mm through the epoxy resin was drilled at 0.5 mm from WE and CE. KCl agar at 1 mol/L was embedded in the hole as a salt bridge. The bottom of the epoxy resin was connected to a U-shaped tube filled with saturated KCl solution. A saturation calomel electrode (SCE) was placed in the U-shaped tube as the reference electrode.

Prior to the electrochemical test, 5.0 g BTAH was placed in the closed container for 24 h to saturate the space. The three-electrode cell was then quickly placed into the closed container after 150 μL of 0.1 mol/L NaCl solution was spread on its surface, which made 8.4 mg/cm^2 NaCl be left on the surface. When temperature and humidity reached and maintained at the set value, ATEL was formed on the entire electrode surface.

It is very difficult to measure the thickness of the ATEL. We have tried to measure it according to reference [6]. We find that the technique in the reference is effective only when the thickness of TEL is above 10 μm. The thickness of the ATEL in our test cannot be determined by using this technique, which partly proves that the thickness of ATEL is less than 10 μm. What is more, when the thickness of TEL is above 10 μm, liquid film can be observed clearly with the naked eye. However, we see no liquid film on the surface of copper under our test condition with the naked eye, which further proves that the thickness of the ATEL is less than 10 μm.

2.3. Electrochemical measurements

The polarization curves and electrochemical impedance spectroscopy of the three-electrode cell were measured at 90% RH and 50 °C after storage in the closed container for 1 h. The sweep rate of the polarization curves was 0.5 mV/s.

The electrochemical impedance spectroscopy was measured at open circuit potential with a 5 mV AC perturbation at frequency ranging from 100 kHz to 5 mHz with 10 points per decade. The test device and the cell configuration for the EIS measurements were the same as those for the polarization curve tests.

To prove reproducibility, the polarization curve tests and the EIS measurements were repeated three times.

2.4. Characterization of the inhibition film by XPS, ATR-FTIR, and SEM

The specimens with 5 mm × 5 mm × 1 mm dimensions were prepared as described above (2.2). After storage in the closed container at approximately 50 °C and 90% RH for 5 h, the specimens were cleaned with distilled water, dried with a cold air blaster, and then used for surface analysis.

XPS measurements were conducted by using a Multi-lab 2000 XPS system with a monochromatic Mg Kα source and a charge neutralizer. The binding energy scale was referenced to the C1s line of the aliphatic carbon contamination set at 284.6 eV.

ATR-FTIR was obtained by using a nitrogen-purged Bruker Vertex70 FTIR spectrometer. The instrument was programmed to run 128 scans with the background and another 128 scans with the specimens.

Morphologies of the copper surfaces in the absence and in the presence of BTAH were observed by using the SEM (FEI, The Netherlands) at 15.0 kV.

Each test was repeated twice at the same conditions to prove the reproducibility of the results.

2.5. In situ AFM measurement

Fig. 2 shows the *in situ* AFM measurement set-up. The specimens with pre-treated surfaces were mounted on the sample platform and were sealed in a box. An automatic heating coil and water vapour were placed in the box to maintain the environment at 90% RH and 50 °C. BTAH was added into the sealed box through a tube. The AFM measurements were carried out by using a commercial AFM system (SPI3800, Seiko Instruments Inc.).

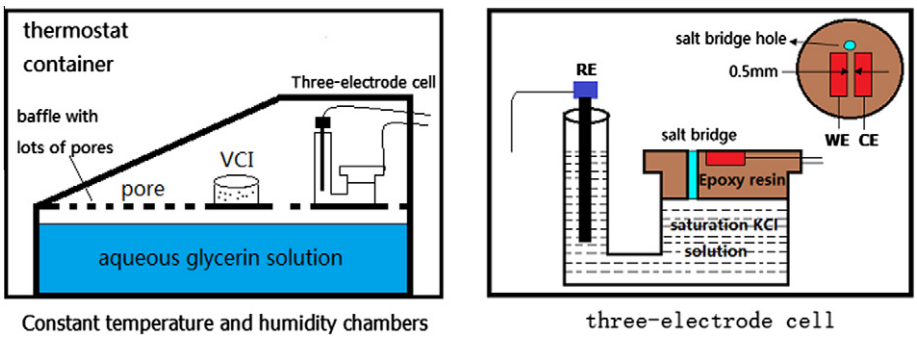

Fig. 1. Schematic diagram of the experimental set-up for the electrochemical test of copper under ATEL.

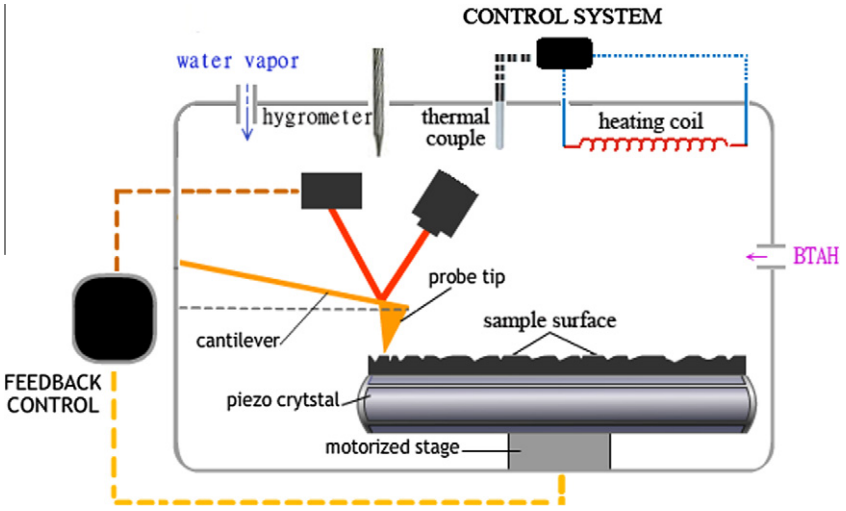

Fig. 2. Experimental set-up for *in situ* AFM measurements.

3. Results

3.1. Polarization curve measurements

Fig. 3 presents the polarization curves for copper under ATEL in the absence and in the presence of BTAH at 90% RH and 50 °C. Fig. 3 indicates that BTAH has a strong inhibition effect on the rate of anodic dissolution of copper by decreasing it at 2–3 orders of magnitudes. This inhibition effect prevails throughout a passive region that extends from the corrosion potential (−220 mV vs. SCE) to the breakdown potential (+430 mV vs. SCE).

The corresponding corrosion potential (E_{corr}), corrosion current density (i_{corr}), anodic Tafel slopes (b_a), and cathodic Tafel slopes (b_c) are listed in Table 1. η is the protection efficiency of BTAH, which is calculated by the following equation [26]

$$\eta = \left(1 - \frac{i'_{corr}}{i_{corr}}\right) \times 100\% \quad (1)$$

where i_{corr} and i'_{corr} are the corrosion current densities of copper in the absence and in the presence of BTAH, respectively.

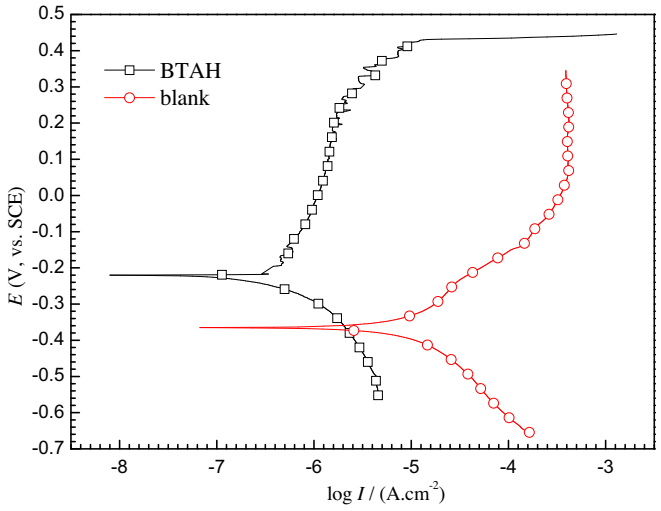

Fig. 3. Potentiodynamic polarization curves of copper under chloride-containing ATEL in the absence and in the presence of BTAH at 90% RH and at 50 °C.

Table 1
Characteristic parameters obtained from polarization curves of copper under chloride-containing ATEL in the absence and in the presence of BTAH at 90% RH and 50 °C.

Sample	E_{corr} (mV, vs. SCE)	i_{corr} (A/cm^2)	b_a (mV/decade)	b_c (mV/decade)	η (%)
Blank	−366	1.25×10^{-5}	69	−117	–
BTAH	−220	6.03×10^{-7}	203	−137	95.2

Table 1 shows that BTAH has a strong inhibition effect on copper corrosion and the inhibition occurs for both the cathode and the anode corrosion.

3.2. EIS measurements

EIS measurements were carried out under ATEL in the absence and in the presence of BTAH at 90% RH and 50 °C. Fig. 4 shows the corresponding Nyquist plots. The Nyquist diagram of copper

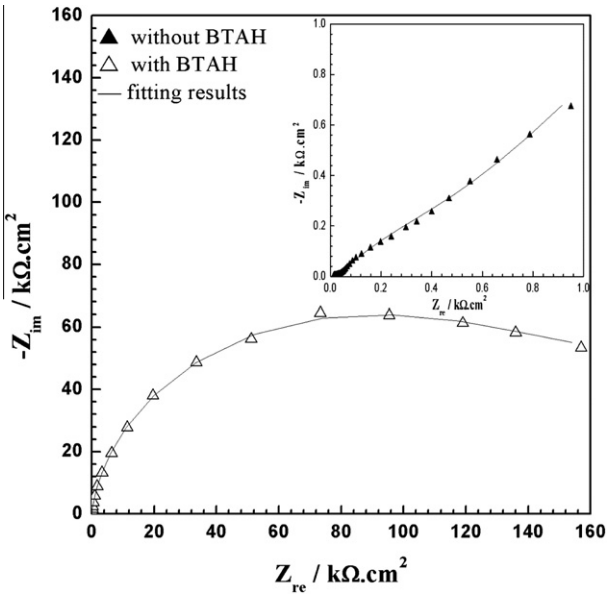

Fig. 4. Nyquist plots measured at E_{corr} for copper under chloride-containing ATEL in the absence and in the presence of BTAH at 90% RH and at 50 °C.

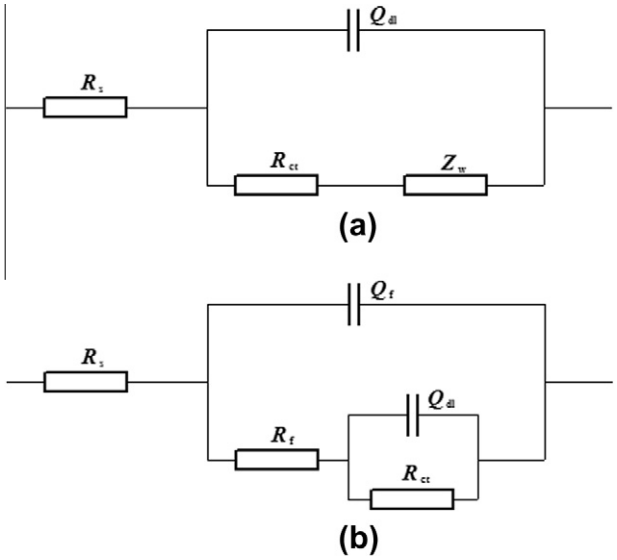

Fig. 5. Equivalent circuits for copper under chloride-containing ATEL in the absence (a) and in the presence (b) of BTAH at 90% RH and at 50 °C.

in the absence of BTAH describes a capacitive arc with high frequency values, which is followed by a straight line at lower frequency values. The straight line at lower frequency values can be ascribed to a diffusion-limited process. In the presence of BTAH, the impedance spectrum switches to double-capacitive semi-circles. The disappearance of the diffusion features in the presence of BTAH indicates that the corrosion reaction is inhibited by BTAH, which makes the diffusion process no longer the control process.

Fig. 5 illustrates the proposed equivalent circuit to quantify the electrochemical parameters. The equivalent circuit shown in Fig. 5(a) is used for fitting EIS data of copper in the absence of BTAH [27,28], while in Fig. 5(b), the equivalent circuit is used for fitting the EIS data of copper in the presence of BTAH [29,30]. In the two equivalent circuits, R_s is the solution resistance; Q_f and Q_{dl} are constant phase elements representing the capacitance of the inhibition film and the double-charged layer, respectively; R_{ct} is the charge-transfer resistance; R_f is the resistance of the inhibition film; and Z_w is the Warburg impedance. The EIS data were fitted well by using the equivalent circuits and the fitting errors were less than 3% for both real and imaginary parts of impedance.

Table 2 lists the fitted parameters attained through EIS data fitting with equivalent circuits. θ in Table 2 is the surface coverage of the surface film, which is calculated according to the following equation [31].

$$\theta = \left(1 - \frac{R_{ct}}{R'_{ct}}\right) \times 100\% \quad (2)$$

where R_{ct} and R'_{ct} are the charge-transfer resistance values of copper in the absence and in the presence of BTAH, respectively.

Table 2
Typical parameters obtained from EIS fitting results of copper under chloride-containing ATEL in the absence and in the presence of BTAH at 90% RH and at 50 °C.

Sample	R_{ct} (Ω cm^2)	Q_{dl} ($s^n\ \Omega^{-1}$ cm^{-2})	R_f (Ω cm^2)	Q_{sam} ($s^n\ \Omega^{-1}$ cm^{-2})	θ (%)
Without BTAH	976.8	5.07×10^{-3}	–	–	–
With BTAH	2.80×10^5	5.93×10^{-6}	61,941	1.05×10^{-6}	99.6

3.3. In situ AFM measurement

Fig. 6 presents the *in situ* AFM topographic image and the phase image of the copper surface during the early stages of corrosion under ATEL in the absence of BTAH. The white particles on the surface, as shown in the topographic image, are salt. No difference can be found with the salt in the AFM topographic image. However, some gray stains around the salt are seen in the AFM phase image, as shown in Fig. 6(b). Higher Cl^- concentration is expected around the salt, which can accelerate and form copper corrosion. The gray stains are defect sites that are undergoing corrosion. During the early corrosion stage, corrosion products are too thin to be detected by the AFM topographic image. However, physical properties, such as hardness, manifest major differences between the defect sites and the non-corroded areas, which can be distinguished by the AFM phase images [32–34].

BTAH was subsequently introduced to the system. One hour later, the force–distance curve measurements were carried out by

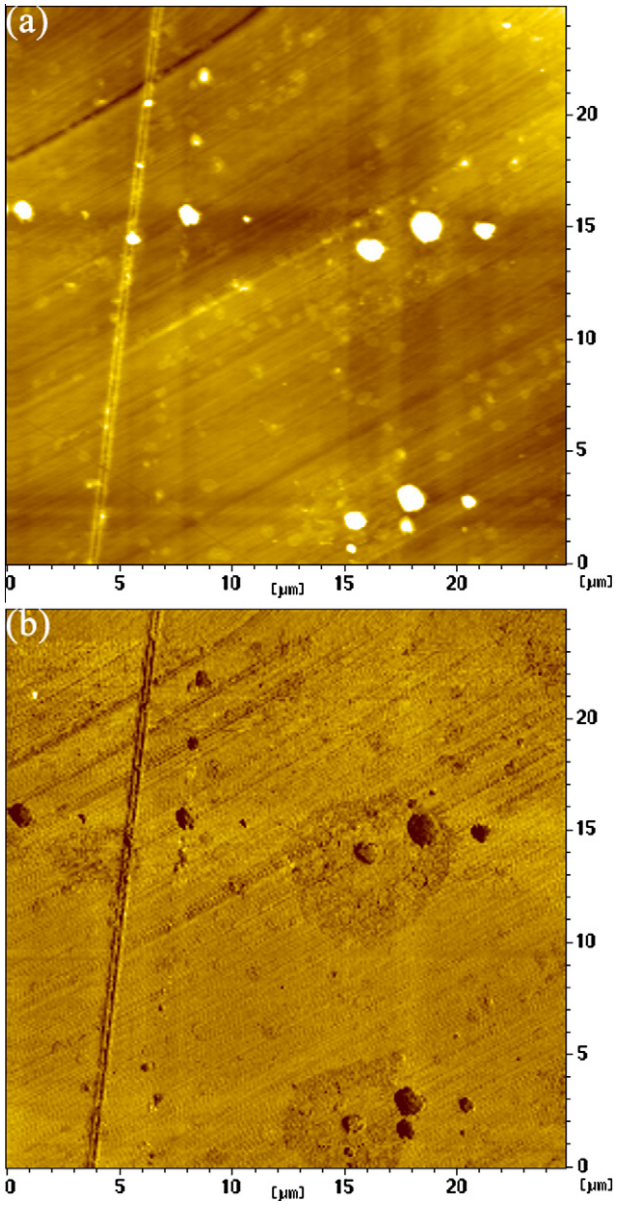

Fig. 6. In situ AFM topographic image (a) and phase image (b) of the copper surface during the early stages of corrosion under chloride-containing ATEL in the absence of BTAH at 90% RH and at 50 °C.

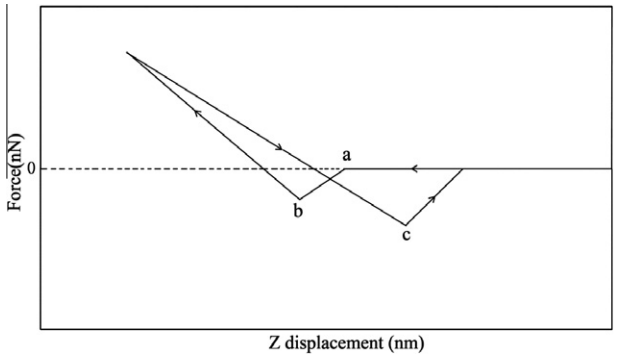

Fig. 7. Schematic representation of a typical force curve of AFM.

using the AFM. The adhesive force between the adsorption film and the solid surface can be directly quantified by measuring the AFM force–distance curve [35]. The measured representative force–distance curve of AFM is presented in Fig. 7. At large tip–sample distances, the force experienced by the tip is null. As the tip approaches the surfaces, it will experience attractive forces (negative) between the region from position a to b. When the attractive forces exceed the spring forces of the cantilever, the tip will jump into contacting with the sample surface at position b, then the repulsive forces (plus) increase. As retracting the tip from the sample, the curve shows a "pull-off" force [36]. When the spring forces of the cantilever exceed the adhesive attraction forces, the tip jumps off contacting from the surface and a maximal adhesive force is detected at point c. Generally, no adhesive force characteristic is recorded on a clean rigid surface in the force–distance curve. However, when the surface is covered by organic film, the adhesive force can be measured because of the adhesive function between the sample and the tip of the probe [35]. To minimize errors due to uncertain factors, the experiments were repeated and 10 force curves were measured in the non-corroded areas and in the defect sites. The results are shown in Fig. 8. The results indicate that adhesion strength in defect sites around the salt is larger than in non-corroded areas, which suggests the presence of more BTAH at defect sites than in other areas.

3.4. SEM analysis

Fig. 9 shows the morphologies of copper under ATEL in the absence and in the presence of BTAH, which were studied by using

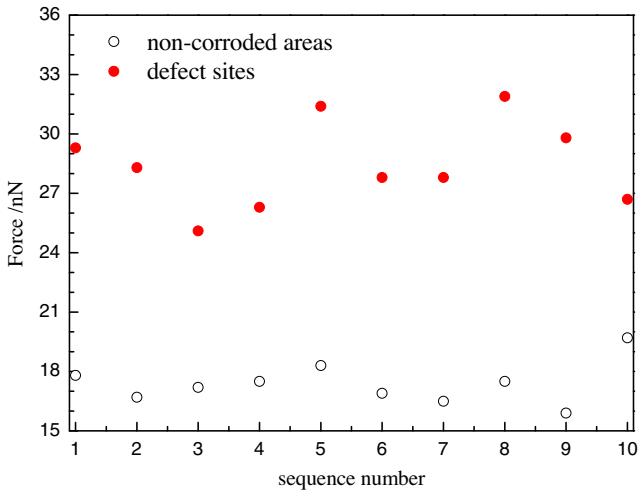

Fig. 8. Adhesion forces measured in non-corroded areas and in defect sites on the copper surface under chloride-containing ATEL in the presence of BTAH at 90% RH and at 50 °C.

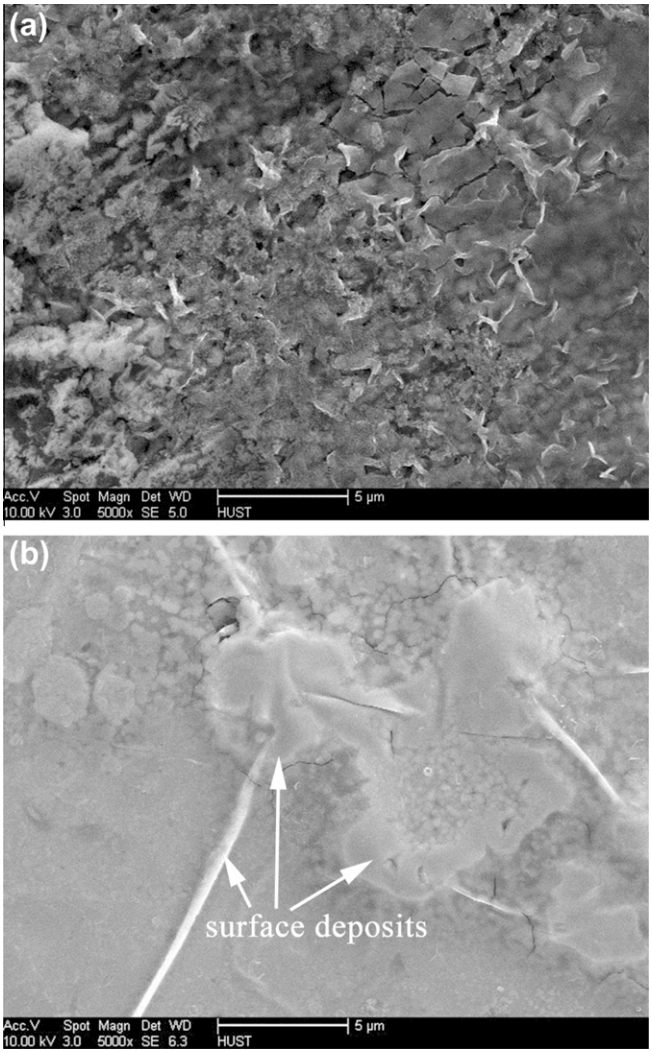

Fig. 9. SEM image of copper under chloride-containing ATEL in the absence (a) and in the presence (b) of BTAH at 90% RH and at 50 °C.

the SEM. In Fig. 9(a), large areas of the copper surface are obviously covered with loose corrosion products in the absence of BTAH. This finding may be an indication that corrosion products easily leave the metal surface and then develop stronger corrosion activity [37]. Table 3 shows the element content deduced from the investigation done with the Energy dispersive X-ray (EDX).

Fig. 9(b) presents the SEM micrograph obtained in the presence of BTAH, which shows a relatively flat surface with a small amount of surface deposits. EDX analysis (Table 3) reveals that surface deposits consist of Cu, O, Cl, C, and N. These elements indicate that surface deposits comprise the inhibition film formed by BTAH with copper. However, no C or N was found at the flat area. The inhibition film may be very thin at the flat area, which is probably a monolayer or a sub-monolayer [19,38,39], and cannot be detected by the EDX.

Table 3
Element content deduced from EDX of copper under chloride-containing ATEL in the absence and in the presence of BTAH at 90% RH and at 50 °C.

Elements	C (wt.%)	N (wt.%)	O (wt.%)	Cl (wt.%)	Cu (wt.%)
Without BTAH	0	0	7.0	3.1	90.3
Deposits	2.1	1.3	7.3	3.3	75.6
Flat area	0	0	0	0	100

3.5. XPS analysis

Fig. 10 shows the XPS spectra of copper under ATEL in the absence and in the presence of BTAH. In the absence of BTAH, the C1s peak at 284.6 eV mainly came from contamination, while the O1s peak at 531.0 eV corresponded to oxygen in Cu_2O [40]. The Cu2p peak at 932.1 eV was attributed to the copper substrate and to Cu_2O that was hardly distinguished by a 0.1 eV binding energy shift [41]. The Cl2p peak at 198.0 eV corresponded to chlorine in CuCl. The XPS spectra indicated that no Cu(II) was present in the corrosion products, which further proved that the corrosion products were CuCl and Cu_2O.

For the XPS spectra of copper at the flat area under ATEL in the presence of BTAH, the C1s peak was very strong and mainly came from the inhibition films. The N1s peak at 399.5 eV was a sign of the formation of the inhibition film by BTAH and copper. The N1s peak corresponded to the N atom in the BTAH molecule, while the N atom interacted with the Cu surface [11]. Cu2p at 932.4 eV can be attributed to the copper substrate.

These results demonstrate that BTAH was successfully absorbed on the flat area and interacted with copper to form the inhibition film. The XPS spectra imply that no O and Cl exist at the flat area in the presence of BTAH. This finding indicates the absence of corrosion products at the flat area and the interaction of BTAH with clean Cu(0) to form the protective film at the non-corroded area.

3.6. ATR-FTIR measurements

The FTIR analysis of the copper specimens under ATEL in the absence and in the presence of BTAH was carried out between 500 and 4000 cm^{-1}. Fig. 11 shows the spectrum.

For specimens in the absence of BTAH, no characteristic peaks were observed besides water. For specimens in the presence of BTAH, the bands that appeared at 3452–3394 and 3238–3091 cm^{-1} were assigned to hydrogen bands O–H, N–H, and C–H [42,43]. Hydrogen bands O–H and N–H may be due to the small amount of water adsorbed in the film and to the inhibitor molecules by physical adsorption. The bands at 1597 and 1446 cm^{-1} were due to C=C stretching of the aromatic ring carbons. Regions at 1348 cm^{-1}, 1309 cm^{-1}, and 1267 cm^{-1} were classified to C–N stretching vibration [44]. 747 cm^{-1} was designated to the phenyl ring out-of-plane bending vibration, while 567–610 cm^{-1} was designated to Cu–N stretching vibration [45,46].

These results indicate that BTAH successfully adsorbed on the copper substrate via the N atom in the molecule.

4. Discussion

4.1. Absence of BTAH

The EDX results reveal that the corrosion products of copper under ATEL in the absence of BTAH mainly consist of Cu, O, and small amounts of Cl. The XPS results indicate that no Cu(II) is present in the corrosion products. Therefore, the corrosion products are primarily Cu_2O and CuCl. Due to the activation effect of chloride ions, the anodic dissolution for the blank specimen under ATEL proceeded according to the following equations [6,37,47].

$$Cu + Cl^- \rightarrow CuCl_{ads} + e^- \quad (3)$$

$$CuCl_{ads} + Cl^- \rightarrow CuCl_2^- \quad (4)$$

$$Cu + 2Cl^- \rightarrow CuCl_2^- + e^- \ (\text{slow}) \quad (5)$$

Meanwhile, copper oxide formed due to the hydrolysis of $CuCl_2^-$ is expressed as

$$CuCl_2^- + \frac{1}{2}H_2O \rightarrow \frac{1}{2}Cu_2O + 2Cl^- + H^+ \quad (6)$$

Since oxygen in the air can easily permeate ATEL to the copper surface, the cathodic reaction is

$$\frac{1}{2}O_2 + H_2O + 2e^- \rightarrow 2OH^- \quad (7)$$

The EIS results imply that diffusion controls the corrosion of copper under ATEL. The anodic dissolution of copper and the cathodic oxygen reduction reactions take place simultaneously on the copper surface. The diffusion process may be due to either the transportation of soluble copper species ($CuCl_2^-$) or the diffusion of dissolved oxygen to the copper surface. Given that ATEL is an extremely thin layer, oxygen in the air can easily permeate ATEL to the copper surface. The diffusion process of $CuCl_2^-$ probably controls the corrosion of copper under ATEL. The polarization curve for copper under ATEL in the absence of BTAH (Fig. 3) consists of a limiting-current region at the anode part, which further

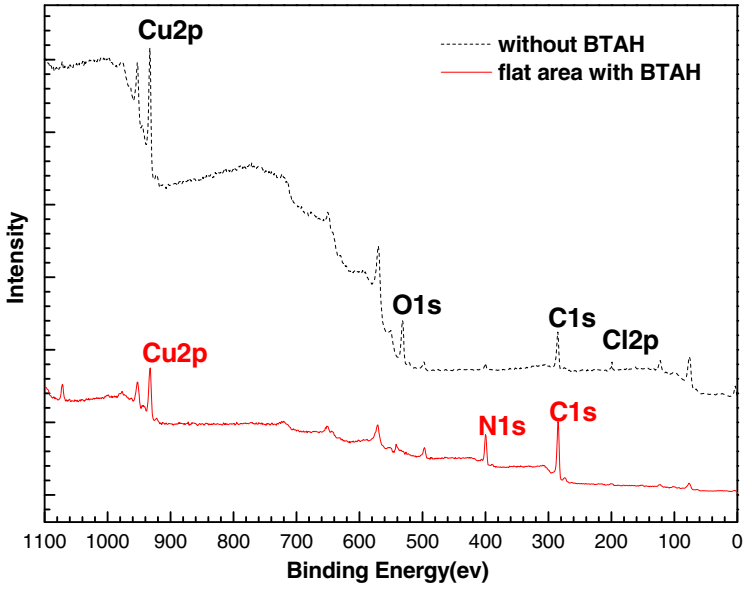

Fig. 10. XPS spectra of copper under chloride-containing ATEL in the absence and in the presence of BTAH at 90% RH and at 50 °C.

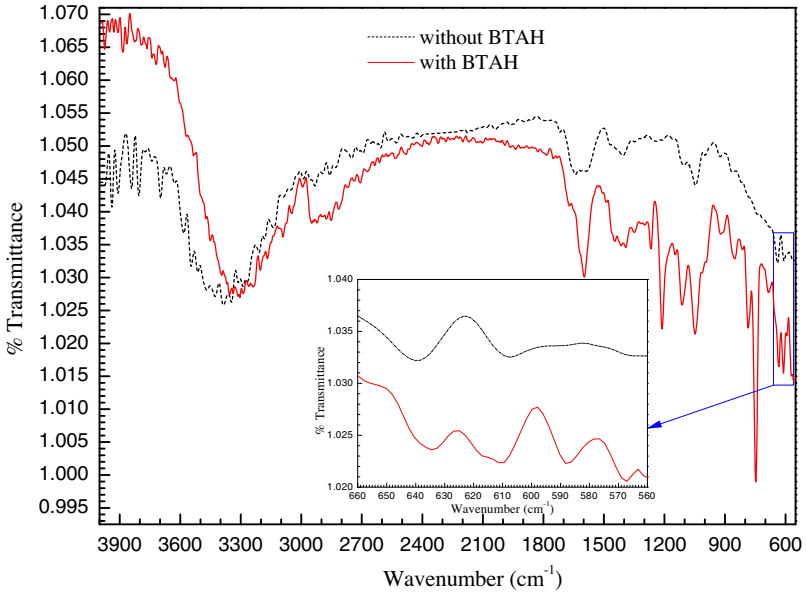

Fig. 11. FTIR spectra of copper under chloride-containing ATEL in the absence and in the presence of BTAH at 90% RH and at 50 °C.

proves the control of $CuCl_2^-$ mass transport in the corrosion process. The diffusion control process of copper under ATEL is unlike that in TEL, in which the diffusion control process is the transport of oxygen through the copper-solution interface [6].

4.2. Presence of BTAH

The increase of absolute value of anodic Tafel slope and cathodic Tafel slope in the presence of BTAH suggests that BTAH is a mixed-type inhibitor for copper. The obvious increase of the anode Tafel slope value and the positive shifts of E_{corr} in the presence of BTAH are due to the exertion of more effective actions on the anodic reaction than on the cathodic reaction [48]. The charge-transfer resistance R_{ct}, which is inversely proportional to the corrosion rate, significantly increases in the presence of BTAH. This observation denotes the strong inhibition effect of BTAH on copper under ATEL. The decrease of Q_{dl} indicates the replacement of water on copper surface by inhibitor. The relative big value of R_f proves that the inhibition film is very compact. Surface coverage of the surface film is 99.6%, which indicates the surface is almost entirely covered with inhibition film.

The AFM phase images reveal that some defect sites are in high Cl^- concentration areas during the initial stages. This finding is attributed to the formation of Cu_2O and $CuCl_2^-$. C–N and Cu–N stretching vibrations from the ATR-FTIR results indicate that BTAH is successfully adsorbed on the copper substrate. The AFM force–distance curves prove that more BTAH are present at defect sites than in other areas. The SEM micrograph shows that BTAH combines with Cu(I) in defect sites, and forms surface deposits. The EDX results prove that the products comprise the inhibition film formed by BTAH with copper. No C or N is found at the flat area by the EDX, but both C and N are found at the flat area by the XPS. This finding suggests the very thin characteristic of the inhibition film at the flat area may be a monolayer or a sub-monolayer. However, the inhibition films at defect areas are multi-layer films. If Cu(0) is oxidized to Cu(I) or Cu(II), there will exist Cl or O element. According to the XPS spectra, neither O nor Cl elements is detected at the flat area. The XPS results prove that BTAH interacts with Cu(I) via the N atom in its molecule in defect sites and interacts with Cu(0) in the flat area.

For specimens in the presence of BTAH under Cl^--containing ATEL, $CuCl_2^-$ is formed based on reactions (3)–(5) in defect sites, then $[Cu(I)BTA]_n$ complex is formed via the following reaction

$$n\mathrm{CuCl_2^-} + n\mathrm{BTAH} \rightarrow [\mathrm{Cu\text{-}BTA}]_n + 2n\mathrm{Cl^-} + n\mathrm{H^+} \quad (8)$$

Fig. 12 shows the molecule structure of $[Cu–BTA]_n$.

Meanwhile, Cu_2O is also formed in defect sites through the hydrolysis of $CuCl_2^-$ (reaction (6)).

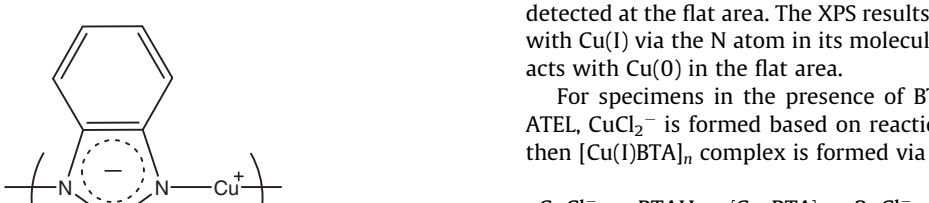

Fig. 12. Molecule structure of $[Cu\text{-}BTA]_n$.

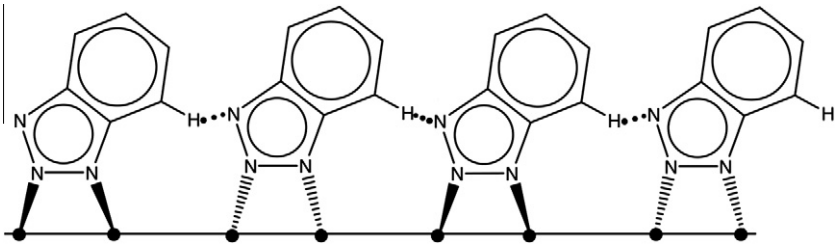

Fig. 13. Molecule structure of Cu(0)-BTAH.

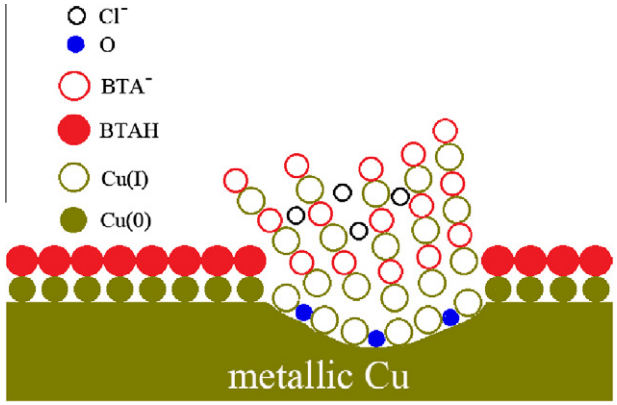

Fig. 14. Adsorption model of BTAH on the copper surface under chloride-containing ATEL in the presence of BTAH at 90% RH.

For specimens in the presence of BTAH under Cl^--containing ATEL, the Cu(0)–BTAH complex is formed at the flat area via the following reaction

$$BTAH + Cu(0) \rightarrow Cu(0)\text{—}BTAH \quad (9)$$

Fig. 13 shows the molecule structure of Cu(0)–BTAH [19].

The cathodic reaction of copper in the presence of BTAH involves the reduction of oxygen (reaction (7)).

Fig. 14 presents the adsorption model of BTAH on the copper surface. BTAH quickly reacts with Cu(0) and forms a strong protective layer in the non-corroded area [49]. The layer is very thin and is presumably a single monolayer [50–52]. However, BTAH reacts with Cu(I) and forms a thick and protective polymeric $[Cu^+BTA^-]_n$ complex [53,54]. The Cu_2O layer is a necessary substrate for the formation of $[Cu(I)BTA]_n$ complex [55–57], hence, the Cu_2O substrate is present under polymeric $[Cu^+BTA^-]_n$ complex [58–61].

5. Conclusions

The corrosion process of copper under ATEL in the absence of BTAH is mainly controlled by $CuCl_2^-$ diffusion. The corrosion products are $CuCl_2^-$ and Cu_2O. BTAH acts as a mixed corrosion inhibitor of copper under ATEL and mainly inhibits anodic reaction. BTAH quickly interacts with Cu(0) via the N atom to form a thin protective film in non-corroded areas and with Cu(I) via the N atom to form a thick polymeric $[Cu^+BTA^-]_n$ complex on the Cu_2O substrate in defect sites.

Acknowledgements

The authors acknowledge the support of the National Natural Science Foundation of China (Grant No. 51101066) and the Analytical and Testing Centre of the Huazhong University of Science and Technology.

References

[1] H.L. Huang, Z.H. Dong, Z.Y. Chen, X.P. Guo, The effects of Cl^- ion concentration and relative humidity on atmospheric corrosion behaviour of PCB–Cu under adsorbed thin electrolyte layer, Corrosion Science 53 (2011) 1230–1236.
[2] W.J. Liu, F.H. Cao, A.N. Chen, L.R. Chang, J.Q. Zhang, C.N. Cao, Corrosion behaviour of AM60 magnesium alloys containing Ce or La under thin electrolyte layers. Part 1: microstructural characterization and electrochemical behaviour, Corrosion Science 52 (2010) 627–638.
[3] P.B.P. Phipps, D.W. Rice, Corrosion Chemistry, in: R.F. Gould (Ed.), American Chemical Society, Washington, DC, 1979, p. 235.
[4] X.N. Liao, F.H. Cao, A.N. Chen, W.J. Liu, J.Q. Zhang, C.N. Cao, In-situ investigation of atmospheric corrosion behavior of bronze under thin electrolyte layers using electrochemical technique, Transactions of Nonferrous Metals Society of China 22 (2012) 1239–1249.
[5] R. Montoya, M.L. Escudero, M.C. García-Alonso, Effect of impurities and electrolyte thickness on degradation of pure magnesium: a finite element study, Materials Science and Engineering: B 176 (2011) 1807–1811.
[6] X.N. Liao, F.H. Cao, L.Y. Zheng, W.J. Liu, A.N. Chen, J.Q. Zhang, C.N. Cao, Corrosion behaviour of copper under chloride-containing thin electrolyte layer, Corrosion Science 53 (2011) 3289–3298.
[7] M.S. Venkatraman, I.S. Cole, B. Emmanuel, Model for corrosion of metals covered with thin electrolyte layers: pseudo-steady state diffusion of oxygen, Electrochimica Acta 56 (2011) 7171–7179.
[8] A.Q. Fu, X. Tang, Y.F. Cheng, Characterization of corrosion of X70 pipeline steel in thin electrolyte layer under disbonded coating by scanning Kelvin probe, Corrosion Science 51 (2009) 186–190.
[9] H.L. Huang, X.P. Guo, G.A. Zhang, Z.H. Dong, The effects of temperature and electric field on atmospheric corrosion behaviour of PCB-Cu under absorbed thin electrolyte layer, Corrosion Science 53 (2011) 1700–1707.
[10] A. Subramania, A.R. Sathiya Priya, T. Vasudevan, Diethylamine phosphate as VPI for steel components, Materials Chemistry and Physics 100 (2006) 193–197.
[11] D.Q. Zhang, Z.X. An, Q.Y. Pan, L.X. Gao, G.D. Zhou, Volatile corrosion inhibitor film formation on carbon steel surface and its inhibition effect on the atmospheric corrosion of carbon steel, Applied Surface Science 253 (2006) 1343–1348.
[12] C.H. Liang, C.J. Yang, N.B. Huang, Tarnish protection of silver by octadecanethiol self-assembled monolayers prepared in aqueous micellar solution, Surface and Coatings Technology 203 (2009) 1034–1044.
[13] R. McConnell, Volatile corrosion inhibitors offer effective protection for processing and shipment of metal-based products, Metal Finishing 106 (2008) 23–27.
[14] D.M. Bastidas, E. Cano, E.M. Mora, Volatile corrosion inhibitors: a review, Anti-Corrosion Methods and Materials 52 (2005) 71–77.
[15] J.M. Bastidas, E.M. Mora, S. Feliu, Protective action of two vapour phase inhibitors on the corrosion of mild steel, Werkstoffe und Korrosion 41 (1990) 343–347.
[16] S.M. Milić, M.M. Antonijević, Some aspects of copper corrosion in presence of benzotriazole and chloride ions, Corrosion Science 51 (2009) 28–34.
[17] M.M. Antonijević, S.M. Milić, M.B. Petrović, Films formed on copper surface in chloride media in the presence of azoles, Corrosion Science 51 (2009) 1228–1237.
[18] M.M. Antonijević, S.M. Milić, Electrochemical behaviour of Cu24Zn5Al alloy in alkaline medium in the presence of chloride ions and benzotriazole, Materials Chemistry and Physics 118 (2009) 385–391.
[19] M. Finšgar, I. Milošev, Inhibition of copper corrosion by 1,2,3-benzotriazole: a review, Corrosion Science 52 (2010) 2737–2749.
[20] T. Koseca, A. Legata, I. Milošev, The comparison of organic protective layers on bronze and copper, Progress in Organic Coatings 69 (2010) 199–206.
[21] J. Izquierdo, J. José Santanal, S. González, R.M. Souto, Uses of scanning electrochemical microscopy for the characterization of thin inhibitor films on reactive metals: The protection of copper surfaces by benzotriazole, Electrochimica Acta 55 (2010) 8791–8800.
[22] J.P. Zeng, J.Y. Zhang, X.D. Gong, Molecular dynamics simulation of interaction between benzotriazoles and cuprous oxide crystal, Computational and Theoretical Chemistry 963 (2011) 110–114.
[23] T. Simbeck, S. Thomaier, C. Stock, E. Riedl, H.J. Gores, Measurement of adsorption kinetics of benzotriazole on copper surfaces via impedance scanning quartz crystal microbalance studies, Electrochemistry Communications 13 (2011) 803–805.
[24] G. Danick, P. Michel, S. Stephan, Inhibition of cobalt active dissolution by benzotriazole in slightly alkaline bicarbonate aqueous media, Electrochimica Acta 52 (2007) 4927–4941.
[25] Standard Practice for Maintaining Constant Relative Humidity by Means of Aqueous Glycerin Solutions, ASTM, D 5032±97 (Reapproved 2003).
[26] D.Q. Zhang, P.H. Liu, L.X. Gao, H.G. Joo, K.Y. Lee, Photosensitive self-assembled membrane of cysteine against copper corrosion, Materials Letters 65 (2011) 1636–1638.
[27] W.J. Guo, S.H. Chen, B.D. Huang, H.Y. Ma, X.G. Yang, Protection of self-assembled monolayers formed from triethyl phosphate and mixed self-assembled monolayers from triethyl phosphate and cetyltrimethyl ammonium bromide for copper against corrosion, Electrochimica Acta 52 (2006) 108–113.
[28] S. Li, S. Chen, S. Lei, H. Ma, R. Yu, D. Liu, Investigation on some Schiff bases as HCl corrosion inhibitors for copper, Corrosion Science 41 (1999) 1273–1287.
[29] D. Gopi, K.M. Govindaraju, V. Collins Arun Prakash, D.M. Angeline Sakila, L. Kavitha, A study on new benzotriazole derivatives as inhibitors on copper corrosion in ground water, Corrosion Science 51 (2009) 2259–2265.
[30] T. Kosec, D.K. Merl, I. Milošev, Impedance and XPS study of benzotriazole films formed on copper, copper–zinc alloys and zinc in chloride solution, Corrosion Science 50 (2008) 1987–1997.
[31] V. Ganesh, S.K. Pal, S. Kumar, V. Lakshminarayanan, Self-assembled monolayers (SAMs) of alkoxycyanobiphenyl thiols on gold surface using a lyotropic liquid crystalline medium, Electrochimica Acta 52 (2007) 2987–2997.
[32] V.K. Shukla, S. Kumar, Investigations of environmental induced effects on AlQ3 thin films by AFM phase imaging, Applied Surface Science 253 (2007) 6848–6853.

[33] J.M. Kima, H.S. Jung, J.W. Park, H.Y. Lee, T. Kawaia, AFM phase lag mapping for protein–DNA oligonucleotide complexes, Analytica Chimica Acta 525 (2004) 151–157.
[34] H. Liu, S.Y. Fu, J.Y. Zhu, H. Li, H.Y. Zhan, Visualization of enzymatic hydrolysis of cellulose using AFM phase imaging, Enzyme and Microbial Technology 45 (2009) 274–281.
[35] J.E. Qu, X.P. Guo, Z.Y. Chen, Adsorption behavior of dodecylamine on copper-nickel alloy surface in NaCl solutions studied by electrochemical methods and AFM, Materials Chemistry and Physics 93 (2005) 388–394.
[36] Y.F. Dufrêne, C.J.P. Boonaert, H.C. van der Mei, H.J. Busscher, P.G. Rouxhet, Probing molecular interactions and mechanical properties of microbial cell surfaces by atomic force microscopy, Ultramicroscopy 86 (2001) 113–120.
[37] G. Gao, C.H. Liang, Some B-amino alcohols compounds as green volatile corrosion inhibitors for brass, Journal of the Electrochemical Society 154 (2007) 144–151.
[38] J.F. Walsh, H.S. Dhariwal, A. Gutiérrez-Sosaa, P. Finettia, C.A. Muryna, N.B. Brookesb, R.J. Oldmanc, G. Thorntona, Probing molecular orientation in corrosion inhibition via a NEXAFS study of benzotriazole and related molecules on Cu(100), Surface Science 415 (1998) 423–432.
[39] J.J. Kester, T.E. Furtak, A.J. Bevolo, Surface enhanced raman scattering in corrosion science. benzotriazole on copper, Journal of the Electrochemical Society 129 (1982) 1716–1719.
[40] G. Beamson, D. Briggs, High Resolution XPS of Origanic Polymers, The Scienta ESCA 300 Database, Wiley, Chichester, 1992.
[41] Y.Q. Feng, W.K. Teo, K.S. Siow, Z.Q. Gao, K.L. Tan, A.K. Hsieh, Corrosion protection of copper by a self-assembled monolayer of alkanethiol, Journal of the Electrochemical Society 144 (1997) 55–64.
[42] P. Hao, Y. Chen, T. Xiao, W.H. Sun, Iron(III) complexes bearing 2-(benzimidazole)-6-(1-aryliminoethyl)pyridines: Synthesis, characterization and their catalytic behaviors towards ethylene oligomerization and polymerization, Journal of Organometallic Chemistry 695 (2010) 90–95.
[43] B. Maria Antoaneta, A. Daniel B, S. Nagahiro, S. Mehmet, T. Osamu, Attenuated total reflectance spectroscopy of simultaneous processes: corrosion inhibition of cuprous oxide by benzotriazole, Applied Surface Science 254 (2008) 2960–2966.
[44] V. Krishnakumar, R. Ramasamy, Scaled quantum chemical studies of the structure and vibrational spectra of 2-(methylthio) benzimidazole, Spectrochimica Acta A 62 (2005) 570–577.
[45] L.P. Lu, M.L. Zhu, P. Yang, Crystal structure and nuclease activity of mono(1,10-phenanthroline) copper complex, Journal of Inorganic Biochemistry 95 (2003) 31–36.
[46] Y. Li, L.P. Lu, M.L. Zhu, Q.M. Wang, C.X. Yuan, Potent inhibition of protein tyrosine phosphatases by copper complexes with multi-benzimidazole derivatives, Biometals 24 (2011) 993–1004.
[47] D.Q. Zhang, L.X. Gao, G.D. Zhou, Inhibition of copper corrosion by bis-(1-benzotriazolymethylene)-(2,5-thiadiazoly)-disulfide in chloride media, Applied Surface Science 225 (2004) 287–293.
[48] S.S. Abd El-Rehim, Magdy A.M. Ibrahim, K.F. Khaled, 4-Aminoantipyrine as an inhibitor of mild steel corrosion in HCl solution, Journal of Applied Electrochemistry 29 (1999) 593–599.
[49] G. Xue, J. Ding, P. Lu, J. Dong, SERS, XPS, and electroanalytical studies of the chemisorption of benzotriazole on a freshly etched surface and an oxidized surface of copper, The Journal of Physical Chemistry 95 (1991) 7380–7384.
[50] B.S. Fang, C.G. Olson, D.W. Lynch, A photoemission study of benzotriazole on clean copper and cuprous oxide, Surface Science 176 (1986) 476–490.
[51] J.O. Nilsson, C. Tornkvist, B. Liedberg, Photoelectron and infrared reflection absorption spectroscopy of benzotriazole adsorbed on copper and cuprous oxide surfaces, Applied Surface Science 37 (1989) 306–326.
[52] N. Morito, W. Suetaka, Infrared reflection studies of the oxidation of copper and the inhibition by benzotriazole, Journal of the Japan Institute of Metals 36 (1972) 1131–1140.
[53] T. Hashemi, C.A. Hogarth, The mechanism of corrosion inhibition of copper in NaCl solution by benzotriazole studied by electron spectroscopy, Electrochimica Acta 33 (1988) 1123–1127.
[54] D. Chadwick, T. Hashemi, Adsorbed corrosion inhibitors studied by electron spectroscopy: benzotriazole on copper and copper alloys, Corrosion Science 18 (1978) 39–51.
[55] F. Mansfeld, T. Smith, Tafel slopes and corrosion rates from polarization resistance measurements, Corrosion 29 (1973) 397–402.
[56] G.W. Poling, Reflection infra-red studies of films formed by benzotriazole on Cu, Corrosion Science 10 (1970) 359–370.
[57] G. Lewis, Adsorption of benzotriazole onto cuprous oxides surface – an electrode impedance study, Corrosion 34 (1978) 424–428.
[58] D. Tromans, R. Sun, Anodic polarization behavior of copper in aqueous chloride/benzotriazole solutions, Journal of the Electrochemical Society 138 (1991) 3235–3244.
[59] J.H. Chen, Z.C. Lin, S. Chen, L.H. Nie, S.Z. Yao, An XPS and BAW sensor study of the structure and real-time growth behaviour of a complex surface film on copper in sodium chloride solutions (pH = 9), containing a low concentration of benzotriazole, Electrochimica Acta 43 (1998) 265–274.
[60] A.D. Modestov, G.D. Zhou, Y.P. Wu, T. Notoya, D.P. Schweinsberg, A study of the electrochemical formation of Cu(I)-BTA films on copper electrodes and the mechanism of copper corrosion inhibition in aqueous chloride/benzotriazole solutions, Corrosion Science 36 (1994) 1931–1946.
[61] V. Brusic, M.A. Frisch, B.N. Eldridge, F.P. Novak, F.B. Kaufman, B.M. Rush, G.S. Frankel, Copper corrosion with and without inhibitors, Journal of the Electrochemical Society 138 (1991) 2253–2259.